Electronic Transport Properties and Nanodevice Designs for Monolayer MoSi$_2$P$_4$

Yifan Gao,[1] Jiabao Liao,[1] Heyan Wang,[1] Yi Wu,[1] Yilian Li,[1] Kun Wang ⊙,[2,3,*] Chunlan Ma ⊙,[4]
Shijing Gong,[5] Tianxing Wang,[1] Xiao Dong,[1] Zhaoyong Jiao,[1] and Yipeng An ⊙[1,†]

[1]*School of Physics, Henan Normal University, Xinxiang 453007, China*

[2]*Department of Physics and Astronomy, Mississippi State University, Mississippi State, Mississippi 39762, USA*

[3]*Department of Chemistry, Mississippi State University, Mississippi State, Mississippi 39762, USA*

[4]*School of Physics and Technology, Suzhou University of Science and Technology, Suzhou 215009, China*

[5]*Department of Physics, East China Normal University, Shanghai 200062, China*

A family of MA_2Z_4 materials has recently inspired great interest due to its exotic geometry and intriguing electronic properties. Here we investigate the electronic transport and photoelectric properties of MoSi$_2$P$_4$ monolayer (MSP ML) that has a small direct gap using first-principles calculations. We design several model nanodevices based on MSP ML, including *p*-*n* junction diodes, *p*-*i*-*n* junction field-effect transistors, and photoelectric transistors. We demonstrate that these MSP-ML-based nanodevices yield superb transport properties, including significant rectifying effect, high electrical anisotropy, pronounced field-effect behavior, strong photoelectric response, and large photovoltaic power. These findings reveal the multifunctional nature of MoSi$_2$P$_4$ monolayer, promising its application as a designer material in next-generation ultrathin flexible semiconductor nanodevices.

I. INTRODUCTION

Since the successful exfoliation of monolayer graphene from graphite, two-dimensional (2D) materials have attracted extensive interest due to their ultrathin geometry and excellent physical and material properties [1–9]. Various 2D semiconductor materials containing transition metals have been theoretically predicted and prepared in experiments, including transition metal dichalcogenides [10], CrI$_3$ [11], Cr$_2$S$_3$ [12], GeSe [13], Nb$_2$SiTe$_4$ [14–16], WSe$_2$|HfSe$_2$ [17], NbSe [18], and MnBi$_2$Te$_4$ [19,20]. Given the diverse morphologies and phases of these 2D monolayers, further attention has been directed to examining their electronic and optoelectronic applications [21,22], such as transistor-type devices [23,24] and optoelectronic nanodevices [25], as well as their utilization in flexible electronic devices harnessing phase transition effects [26].

Recently, types of 2D layered nonmagnetic semiconductor materials, MoSi$_2$N$_4$ and WSi$_2$N$_4$, often prepared using chemical vapor deposition (CVD) methods, were found to yield high carrier mobility, good mechanical strength, and excellent environmental stability and optical properties [27–29]. The detailed electronic structure and spin

polarization properties of MoSi$_2$N$_4$ as a function of material thickness were revealed by density functional theory (DFT) calculations [30–32]. It has also been predicted that van der Waals heterojunctions containing MoSi$_2$N$_4$, such as MoSi$_2$N$_4$/graphene, can act as high-performance nanodevices [33]. Furthermore, Chen *et al.* recently proposed 72 MA_2Z_4-type stable structures and studied their topological and magnetic properties, greatly expanding the library of the MA_2Z_4-type family materials [34]. Despite the recent progress, the fundamental role and potential application of MA_2Z_4-type family materials in different device architectures remain to be explored. For instance, several critical aspects that need to be thoroughly interrogated include the following. (a) How strong is their electronic transport anisotropy? (b) Can they behave like field-effect transistors (FETs)? (c) What are their photoelectronic properties?

Among various MA_2Z_4-type family materials, MoSi$_2$P$_4$ monolayer (MSP ML) could have efficient photoelectronic properties and low energy consumption due to its small direct band gap, only half that of MoSi$_2$N$_4$ and WSi$_2$N$_4$ monolayers. Here, we systematically investigate the electronic transport and photoelectronic properties of MSP ML via detailed first-principles calculations. We design conceptual 2D nanodevices employing MSP ML as the core transport channel. Specifically, we examine several essential device architectures, including *p*-*n* junction diodes, *p*-*i*-*n* junction field-effect transistors, and phototransistors. We find that when employed in different device systems,

*kw2504@msstate.edu

†ypan@htu.edu.cn

034033-1

MSP ML can yield a wide range of desired transport phenomena, such as rectification, strong electronic anisotropy, field-effect behavior, high photoelectronic response, and photovoltaic effect. These findings reveal the suitability of using MSP ML as a multifunctional building block in future nanoelectronics devices.

II. CALCULATION METHODS

We determine the geometric and electronic structures, transport, and photoelectronic properties of 2D MSP ML using DFT [31,35] and nonequilibrium Green's function methods [36], as implemented in the Atomistix Toolkit code [37–41]. The Perdew-Burke-Ernzerhof (PBE) [42] function of the generalized gradient approximation [43,44] is used to describe the electron exchange and correlation effects. We choose the optimized norm-conserving Vanderbilt pseudopotentials to represent the ionic core of all atoms [45]. The wave functions of valence states are treated as a linear combination of atomic orbitals model. To solve the Poisson equation, we adopt a real-space mesh-grid density cutoff of 55 Ha. Total energy tolerance and residual force on each atom are less than 10^{-6} eV and 10^{-4} eV/Å in the geometric optimization. In the transport calculations, Monkhorst-Pack k-point grids of $1 \times 5 \times 300$ (Z-type) and $1 \times 8 \times 160$ (A-type) are used to sample the Brillouin regions of the electrodes of all MSP ML devices studied in this work.

III. RESULTS AND DISCUSSION

Figures 1(a) and 1(b) illustrate the top and side views of MSP ML, respectively. Each unit cell contains one molybdenum atom, two silicon atoms, and four phosphorus atoms. Mo, Si, and P atoms in $MoSi_2P_4$ are arranged in a hexagonal honeycomb lattice, forming a 2D crystal with space group P_{6m2} (No. 187) [46,47]. From the side view, MSP ML is a covalently bonded crystal with a thickness of 7 atomic layers consisting of the P-Si-P-Mo-P-Si-P sequence. The optimized in-plane lattice parameter **a** of its hexagonal septuple-layer structure is 3.47 Å, with external P—Si bond length $d_{P-Si} = 2.24$ Å, internal Si—P bond length $d_{Si-P} = 2.26$ Å, and P—Mo bond length $d_{P-Mo} = 2.47$ Å. The $MoSi_2P_4$ monolayer has a nonmagnetic ground state based on the total energies obtained by spin polarized and unpolarized calculations. These results are consistent with recent reports [29,47–49].

To examine the structural stability of free-standing MSP ML, we first calculate the phonon spectrum and projected phonon density of states (PDOS), as shown in Fig. 1(c). The MSP ML has no imaginary frequency in the whole Brillouin zone, indicating that it has robust dynamic stability and can maintain a stable free-standing structure without a substrate, consistent with recent reports [29,50]. This suggests that MSP ML can be experimentally prepared using methods adopted in the fabrication of homogeneous
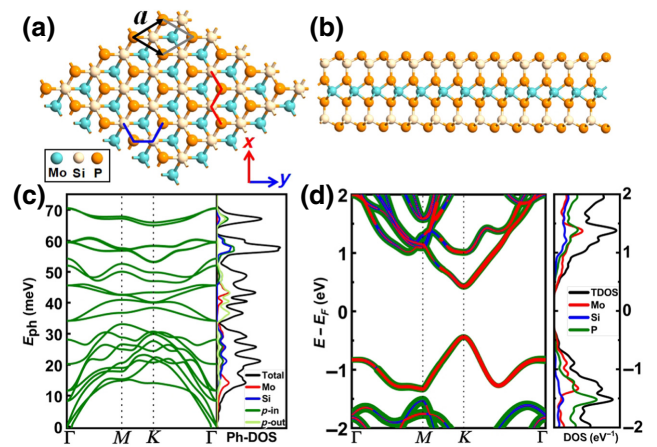

FIG. 1. Schematics of the top (a) and side (b) views of MSP ML. The x and y axes represent the zigzag and armchair directions, respectively. (c) Phonon spectrum and projected PDOS. (d) Element-projected electronic band and DOS. The Fermi level (E_F) is set to zero.

$MoSi_2N_4$ and WSi_2N_4 monolayers, such as CVD. Each unit cell of MSP ML contains 7 atoms, so its phonon spectrum has 21 phonon branches that can be divided into 3 acoustic (A) branches and 18 optical (O) branches [51]. Its phonon spectrum has several small gaps among the O branches, analogous to other 2D monolayers containing transition metals, such as NiI_2 [52], but different from graphene and MoS_2 [53], which has a complex crossing among the O branches. From the PDOS, we find that the low-frequency A branches mainly originate from the harmonic vibration of central Mo atoms, whose contribution reduces to a level similar to those of Si and P atoms with an increase of vibrational frequency. Figure 1(d) shows the element-projected electronic bands and DOS. MSP ML has a direct band gap located at the K point with a value of 0.74 eV, lower than the indirect band gap of $MoSi_2N_4$ ML (approximately 1.94 eV) [27]. Note the gap obtained by the screened hybrid functional of HSE06 [54] is 1.02 eV. Our calculated band gaps obtained by PBE and HSE06 functionals are consistent with previous reports [29]. The projected DOS reveals that the conduction and valence bands near the K point are mainly contributed by the d orbital of Mo atoms.

To gain a deeper insight into the energy-dispersion relationship around the Fermi level (E_F), we examine the lowest conduction and highest valence bands of MSP ML around the Γ point in a three-dimensional view. As depicted in Fig. 2(a), the cone-shaped (funnel-shaped) bands form a robust hexagonal structure at the high-symmetry points. The electron (hole) effective mass of the valence band maximum (conduction band minimum) at the K point is $-0.35m_e$ ($0.34m_e$) (m_e is the free-electron mass), greater than that of the $MnBi_2Te_4$ monolayer [20]. From the projection of energy dispersions in the 2D k-space
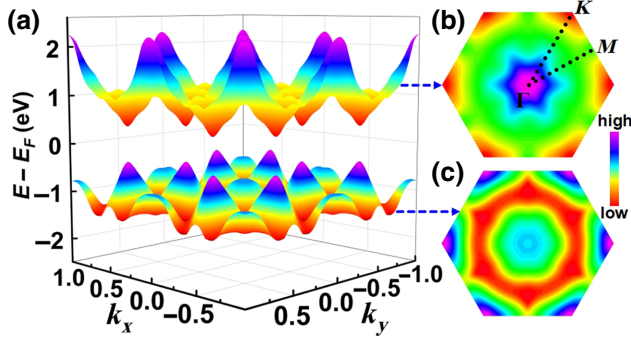
FIG. 2. (a) Three-dimensional views of conduction and valence bands around the Γ point. (b),(c) Two-dimensional projection plots in the first Brillouin zone. The rainbow colormap shows conduction and valence band energy eigenvalues from low (red) to high (purple).

of the first Brillouin zone [Figs. 2(b) and 2(c)], we can see that the energy dispersions become anisotropic when away from the high-symmetry points (i.e., K and Γ points), and their contour maps gradually approach a hexagonal shape when away from the Γ point. In addition, the Fermi velocity at the valence band maximum value shows strong anisotropy and is 1.15×10^4 m/s (1.17 m/s) along the x axis (y axis), smaller than that of the MnBi$_2$Te$_4$ monolayer [20]. Such effect is ascribed to the larger carrier effective mass of MSP ML. The Fermi velocity and effective mass can lead to anisotropic electron transmission under a limited electric field, such as between the x axis (along the zigzag direction) and the y axis (along the armchair direction) [see Fig. 1(a)], as observed in other 2D materials [4,55,56].

A. Rectifying effect of MSP ML p-n junction diode devices

The MoSi$_2$P$_4$ monolayer has larger electron and hole mobility than transition metal disulfide (i.e., WSe$_2$), which are 246 (258) and 1065 (1429) cm^2 V^{-1} s^{-1} along the zigzag (armchair) direction, respectively [49]. This demonstrates that MSP ML could have better applications in electronic and photoelectronic devices. We now investigate the transport properties of MSP-ML-based nanodevices. Figure 3(a) shows a schematic of a p-n junction diode consisting of MSP ML constructed with electrostatic doping with p- and n-type atomic compensation charges [57]. Generally, the effect of electrostatic doping is achieved by either decreasing (p-doping) or increasing (n-doping) the number of electrons of the system with respect to the pristine neutral case. For the atomic compensation charge method used in this work, the extra charge is introduced by modifying the densities of individual atoms. This method has been effectively employed for modeling various nanodevices [9,58–62]. Based on the atomic geometry, there are two possible MSP ML diode structures: Z-type (along the x axis, zigzag along the edges) and
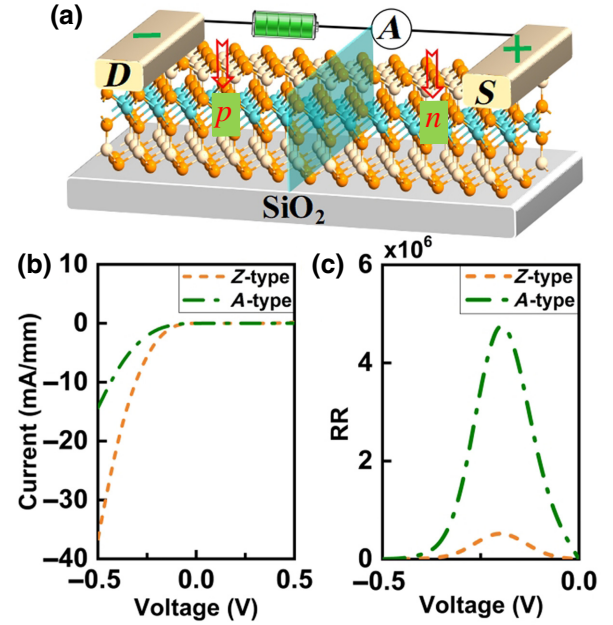

FIG. 3. (a) Schematic, (b) I-V curves, and (c) RR curves of Z- and A-type MSP ML p-n junction diode devices.

A-type (along the y axis, armchair at edges). In this work, we consider a low doping concentration of 3×10^{12} cm^{-2}, equivalent to a normal doping concentration of 10^{19} cm^{-3} in bulk [57,63,64]. Each diode is composed of the drain (D) and source (S) electrodes and the central scattering region (p-n junction). In our electron transport calculations, the periodic p- and n-doped MoSi$_2$P$_4$ unit cells are used to stimulate the D and S electrodes whose length is semi-infinitely extended along the transport direction. When a forward D-S bias V_b is applied, the positive current from the D to S electrode is generated, and vice versa. The current I through the MSP ML diode is determined by the Landauer-Büttiker formula:

$$I(V_b) = \frac{2e}{h} \int_{-\infty}^{\infty} T(E, V_b)[f_D(E - \mu_D) - f_S(E - \mu_S)]dE,$$

$$(1)$$

where e and h are the electron charge and Planck's constant, respectively. $T(E, V_b)$ refers to the transmission coefficient. $f_{D(S)} = \{1 + exp[(E - \mu_{D(S)})/k_B T_{D(S)}]\}^{-1}$ is the Fermi-Dirac distribution function of the D (S) electrode. $\mu_{D(S)}$ and $T_{D(S)}$ indicate the chemical potential and electron temperature, respectively. In this work, the bias voltage range is from -0.5 to 0.5 V with a sampling interval of 0.1 V.

Figure 3(b) displays the current-voltage (I-V) curves of the Z- and A-type MSP ML p-n junction diodes. We can see that both Z- and A-type diodes produce a pronounced current-rectifying effect, that is, the electrical current is prohibited (circuit-off state) under a limited forward bias

but open (circuit-on state) when the reverse bias voltage is applied. The threshold voltage of the circuit-on state for both types of diodes is approximately -0.2 V. The rectification ratio (RR), defined as $RR = |I(-V_b)/I(V_b)|$) for the MSP-ML-based diode, is up to approximately 10^6 [see Fig. 3(c)], comparable to those of some of the lateral transition-metal disulfide heterojunctions [65]. In addition, it is notable that the MSP ML demonstrates remarkable electrical anisotropy. For instance, the currents of Z-type (I_Z) and A-type (I_A) MSP ML p-n junction diodes under -0.5 V are -36.61 and -14.33 mA/mm, respectively [see Fig. 3(b)]. The ratio of current anisotropy $\eta = I_Z/I_A$ is 2.6, much greater than that of other 2D materials [3,4]. Although the Z-type p-n junction diode has higher conductivity under a limited reverse bias, the A-type p-n junction diode yields a greater RR that reaches a peak value at -0.2 V [see Fig. 3(c)]. Note that $MoSi_2P_4$ has a spin-valley coupling with a valley spin splitting of 0.2 eV when considering the spin-orbital coupling effect [66]. This can cause a tiny change to the rectification ratio, while qualitatively remaining the rectifying effect.

In Fig. 4, we plot the transmission spectra and projected local density of states (PLDOS) of the Z- and A-type MSP ML p-n junction diodes at 0, -0.5, and 0.5 V bias voltages. We find that under a reverse bias, the bands of the p- and n-doped terminals shift up and down accordingly [67]. Compared with the PLDOS at equilibrium state (i.e., zero bias), more electron states enter the bias window (BW). As shown in Figs. 4(b) and 4(e), band overlap occurs when a reverse bias reaches a threshold value (i.e., -0.5 V), leading to direct electron tunneling between the conduction bands of the D electrode and the valence bands of the S electrode and generating tunneling current. In contrast, under a forward bias (i.e., 0.5 V), the bands of both D and S electrodes move down and up, respectively [see Fig. 4(c)], which opens up the band gap further and completely inhibits band overlap. As a result,
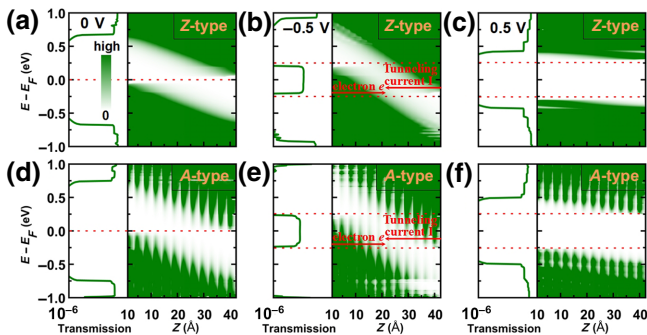
the electron tunneling between the two electrodes is forbidden. Together, the unique band structures of the MSP ML give rise to the strong rectifying effect in the Z-type MSP ML p-n junction diode. The rectifying mechanisms for the A-type diode are similar to those for the Z-type structure [see Figs. 4(d)–4(f)].

Figure 5(a) shows the differential conductance (dI/dV) density curves as a function of bias for the Z- and A-type MSP ML p-n junction diodes, which indicates strong electrical anisotropy of the MSP ML. For instance, the differential conductance density at -0.5 V is 0.21 S/mm for the Z-type diode and 0.09 S/mm for A-type diode. These values are slightly smaller than that of the p-n junction diode of the $MnBi_2Te_4$ monolayer [20]. From the electron transmission spectra of the Z-type diode versus bias voltages depicted in Fig. 5(b), we observe that carrier diffusion only takes place in the reverse BW, not in the forward BW, clearly revealing the rectifying behavior. Figure 5(c) presents the k-dependent electron transmission coefficients $T(E, k)$ under -0.5 V. Near E_F, the elliptical-shaped electron transmission cloud is only observed around the Γ point, and it gradually reduces to zero at the 1/4 position from Γ to $Y(-Y)$. The A-type diode yields very similar device characteristics, but with a smaller values.

B. Field-effect behavior of $MoSi_2P_4$ p-i-n junction transistor devices

Next, we construct MSP ML p-i-n junction FETs [see Fig. 6(a)] and study their field-effect properties. The left and right electrodes of the p-i-n junction are modeled by

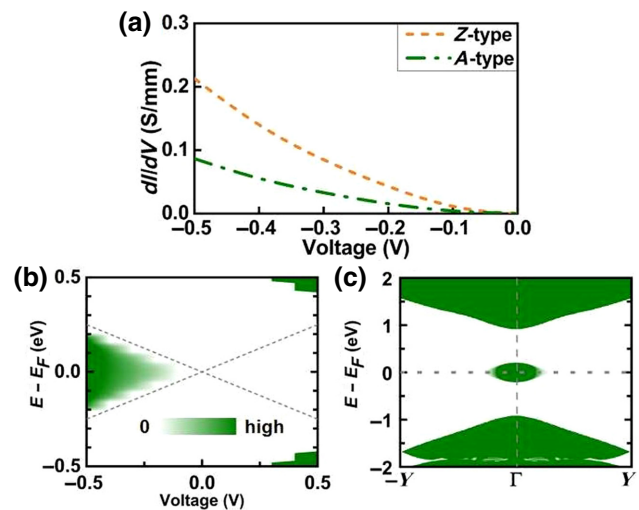FIG. 5. (a) Differential conductance (dI/dV) curves of the Z- and A-type MSP ML p-n junction diodes. (b) Transmission spectra of the Z-type MSP ML p-n junction diode at -0.5 V. (c) The k-dependent transmission coefficients $T(E, k)$ at -0.5 V bias. The colormap shows the data of (b),(c) from 0 (white) to high (green).

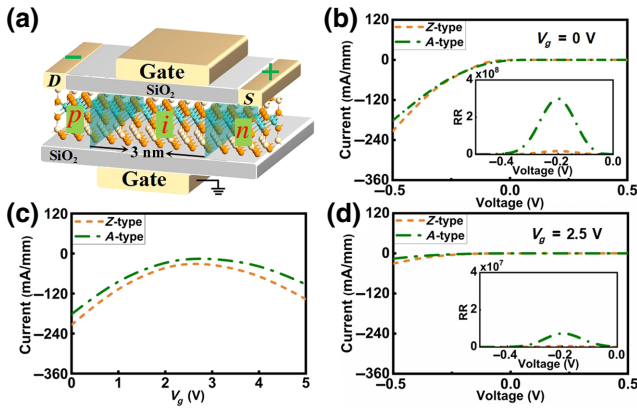FIG. 4. Transmission spectra and PLDOS of Z-type (a)–(c) and A-type (d)–(f) MSP ML p-n junction diodes at (a),(d) 0, (b),(e) -0.5, and (c),(f) 0.5 V bias voltages. The colormap shows the data from 0 (white) to high (green).

FIG. 6. (a) Schematic of the MSP ML *p-i-n* junction field-effect transistor. *I-V* and rectification ratio curves under gate voltages of 0 (b) and 2.5 V (d). (c) Distribution of current at different gate voltages.

p- and *n*-doped unit cells of the MSP ML, respectively. The central scattering region is the *i* MSP ML, i.e., a sub-3-nm FET channel interfaced with two gate electrodes on both the top and bottom sides of the channel. The electrical current through these sub-3-nm *p-i-n* junction FETs is obtained by [68]

$$I(V_b, V_g) = \frac{2e}{h} \int_{-\infty}^{\infty} T(E, V_b, V_g)$$
$$\times [f_D(E - \mu_D) - f_S(E - \mu_S)]dE. \quad (2)$$

Figure 6(b) shows the *I-V* curves of the *Z*- and *A*-type MSP ML *p-i-n* junction FETs under zero gate voltage. Interestingly, strong electrical anisotropy is also observed in the MSP ML *p-i-n* junction FETs. Furthermore, the FET devices exhibit the rectifying effect as well, just as does the *p-n* junction. To further explore the field-effect behavior of the *p-i-n* junctions, we investigate the transport properties under various gate voltages ranging from 0 to 5 V. With an increase of gate voltage, the junction current first decreases and then increases [see Fig. 6(c)]. The minimum current is reached at a gate voltage of 2.5 V [see Fig. 6(d)]. Note that the results for other gate voltages are shown in Fig. 8 within the Appendix. The MSP ML *p-i-n* junctions can yield a superior rectification ratio (larger than 10^6) under suitable gate voltage and display the same trend as their field-effect behavior. These results clearly indicate that the current through the *p-i-n* junction can be effectively regulated by the gate voltage with a high gating efficiency [69], implying that the MSP ML *p-i-n* junction is an excellent candidate for field-effect transistor applications.

C. Photoelectronic properties of MSP ML *p-i-n* junction phototransistors

Finally, we interrogate the photoelectronic properties of MSP ML. Specifically, we construct its *p-i-n* junction phototransistor structure to evaluate its potential application as a photoelectronic device [see Fig. 7(a)]. As illustrated in Fig. 7(b), the optical absorption spectra of MSP ML have the same trend along the *x* axis and *y* axis. The photoconductive channel is opened when the photon energy exceeds its band gap (i.e., 0.74 eV). The absorption strength is continuously enhanced with the increase of photon energy until an inflection point appears at 4.6 eV. Noticeably, the absorption coefficients in the UV region can rise as high as 10^6 cm^{-1}. This large absorption coefficient is even comparable to those of graphene, phosphorene, and molybdenum disulfide [70]. Besides, it has a significantly broad absorption range within the AM1.5 standard. These intriguing photoelectronic properties render MSP ML a
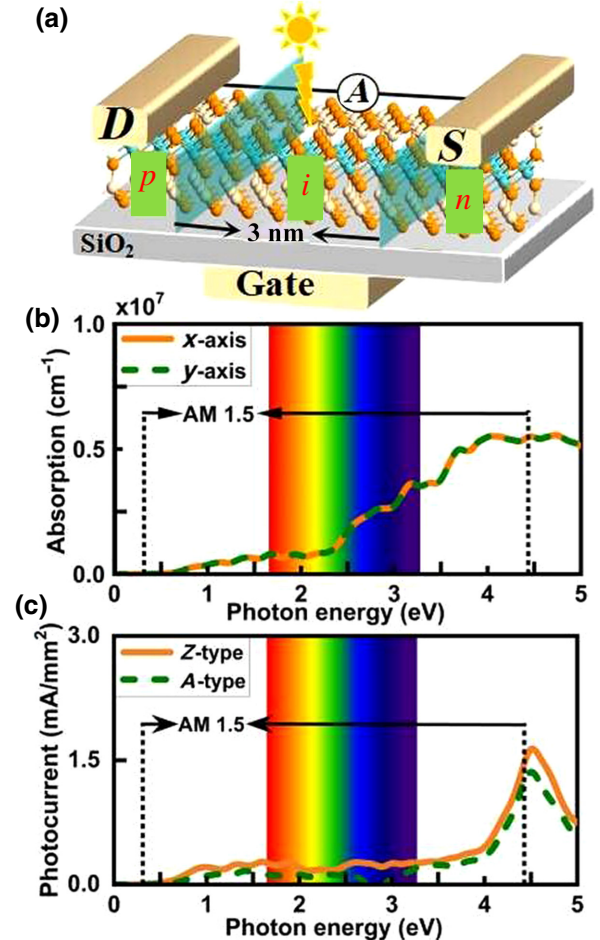

FIG. 7. (a) Schematic of the MSP ML *p-i-n* junction phototransistor. (b) Optical absorption coefficients of MSP ML. (c) Photocurrent density at zero bias (without power) for *Z*- and *A*-type MSP ML *p-i-n* junction phototransistors. The inset spectrum pattern indicates the visible-light region.

promising material for photovoltaic solar cells and photo-electronic devices. Interestingly, we find that the number of layers and band gap are independent of light absorption, which makes the experimental fabrication of 2D optoelectronic devices based on few-layer $MoSi_2P_4$ more convenient [50].

In the simulation of photoelectric transport of the designed phototransistor devices, the incident light is linearly polarized, and the photon energy from 0 to 5 eV is analyzed. When a photon with frequency ω enters the MSP ML transistor and is absorbed, the photogenerated current is described by [59,71]

$$I_\alpha = \frac{2e}{h} \int_{-\infty}^{\infty} \sum_{\beta=D,S} [1 - f_\alpha(E)] f_\beta(E - \hbar\omega) T_{\alpha,\beta}^-(E) - f_\alpha(E)$$
$$\times [1 - f_\beta(E + \hbar\omega)] T_{\alpha,\beta}^+(E) \, dE, \tag{3}$$

where $\alpha = D/S$, and the total photocurrent is obtained by $I_{ph} = I_D - I_S$. Under zero bias (without power), the Z- and A-type MSP ML p-i-n junction phototransistors show a consistent photocurrent trend and magnitude due to their isotropic absorption spectra and the wide peaks in the ultraviolet region. The total photocurrents are calculated to be 1.92 and 1.60 $\mu A/mm^2$ for the Z- and A-type MSP ML p-i-n junction phototransistors, respectively [see Fig. 7(c)]. It is evident that the MSP ML p-i-n junction phototransistors have a strong photoelectric response in the ultraviolet region, similar to that of silicon solar cells [59]. This promises the potential use of MSP ML in ultraviolet photoelectric sensors.

IV. CONCLUSIONS

In conclusion, we theoretically design several nanodevices based on $MoSi_2P_4$ monolayer and study their electronic transport and optoelectronic properties using the density functional theory and nonequilibrium Green's function methods. Our results demonstrate various interesting transport phenomena with superb device performance. Under a normal doping concentration, the p-n junction diode of MSP ML presents a strong rectification effect with high rectification ratio (10^6) and high electrical anisotropy. The p-i-n junction of MSP ML also shows a significant field-effect behavior. The junction current can be suppressed to the minimum value when the gate voltage is 2.5 V. In addition, the rectification ratio of the MSP ML in the p-i-n junction FET structure can exceed that of its p-n junction diode structure. Moreover, it is also found that MSP ML has a wide optical absorption range and strong photoelectric response in the ultraviolet region. The Z- and A-type p-i-n junction phototransistors can generate sizable photocurrents in the ultraviolet region. Overall, our work reveals that the direct-gap semiconductor $MoSi_2P_4$ monolayer is a promising material for a variety of device
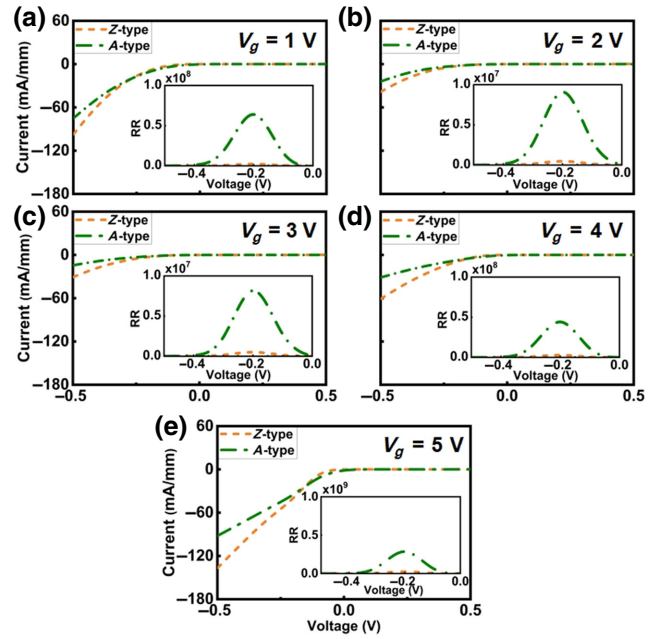

FIG. 8. Transport properties of $MoSi_2P_4$ monolayer p-i-n junction FETs at various gate voltages.

applications, including rectifiers, field-effect transistors, photovoltaic devices, and photoelectric sensors. We also highlight the need for experimental investigation of these proposed device structures in future studies.

APPENDIX

The transport properties of MSP ML p-i-n junction FETs are shown in Fig. 8.

[1] C. Gong, L. Li, Z. Li, H. Ji, A. Stern, Y. Xia, T. Cao, W. Bao, C. Wang, and Y. Wang, Discovery of intrinsic ferromagnetism in two-dimensional van der Waals crystals, Nature **546**, 265 (2017).

[2] K. S. Novoselov, A. K. Geim, S. V. Morozov, D.-E. Jiang, Y. Zhang, S. V. Dubonos, I. V. Grigorieva, and A. A. Firsov,

Electric field effect in atomically thin carbon films, Science **306**, 666 (2004).

[3] Y. An, S. Gong, Y. Hou, J. Li, R. Wu, Z. Jiao, T. Wang, and J. Jiao, MoB$_2$: A new multifunctional transition metal diboride monolayer, J. Phys.: Condens. Matter **32**, 055503 (2019).

[4] Y. An, Y. Hou, H. Wang, J. Li, R. Wu, T. Wang, H. Da, and J. Jiao, Unveiling the Electric-Current-Limiting and Photodetection Effect in Two-Dimensional Hydrogenated Borophene, Phys. Rev. Appl. **11**, 064031 (2019).

[5] Y. An, J. Jiao, Y. Hou, H. Wang, D. Wu, T. Wang, Z. Fu, G. Xu, and R. Wu, How does the electric current propagate through fully-hydrogenated borophene?, Phys. Chem. Chem. Phys. **20**, 21552 (2018).

[6] Y. An, J. Jiao, Y. Hou, H. Wang, R. Wu, C. Liu, X. Chen, T. Wang, and K. Wang, Negative differential conductance effect and electrical anisotropy of 2D ZrB$_2$ monolayers, J. Phys.: Condens. Matter **31**, 065301 (2018).

[7] A. J. Mannix, X. F. Zhou, B. Kiraly, J. D. Wood, D. Alducin, B. D. Myers, X. Liu, B. L. Fisher, U. Santiago, and J. R. Guest, Synthesis of borophenes: Anisotropic, two-dimensional boron polymorphs, Science **350**, 1513 (2015).

[8] J. Arcudia, R. Kempt, M. E. Cifuentes-Quintal, T. Heine, and G. Merino, Blue Phosphorene Bilayer is a Two-Dimensional Metal and an Unambiguous Classification Scheme for Buckled Hexagonal Bilayers, Phys. Rev. Lett. **125**, 196401 (2020).

[9] R. Quhe, Q. Li, Q. Zhang, Y. Wang, H. Zhang, J. Li, X. Zhang, D. Chen, K. Liu, and Y. Ye, Simulations of Quantum Transport in Sub-5-nm Monolayer Phosphorene Transistors, Phys. Rev. Appl. **10**, 024022 (2018).

[10] C. Ataca, H. Sahin, and S. Ciraci, Stable, single-layer MX2 transition-metal oxides and dichalcogenides in a honeycomb-like structure, J. Phys. Chem. C **116**, 8983 (2012).

[11] B. Huang, G. Clark, E. Navarro-Moratalla, D. R. Klein, R. Cheng, K. L. Seyler, D. Zhong, E. Schmidgall, M. A. McGuire, and D. H. Cobden, Layer-dependent ferromagnetism in a van der Waals crystal down to the monolayer limit, Nature **546**, 270 (2017).

[12] Y. Feng, N. Liu, and G. Gao, Spin transport properties in Dirac spin gapless semiconductors Cr2X3 with high Curie temperature and large magnetic anisotropic energy, Appl. Phys. Lett. **118**, 112407 (2021).

[13] Z.-Q. Fan, J. Chen, and X. Jiang, Electrical contacts and tunable rectifications in monolayer GeSe-metal junctions, J. Phys. D: Appl. Phys. **51**, 335104 (2018).

[14] X. Wu, G. Gao, L. Hu, and D. Qin, 2D Nb$_2$SiTe$_4$ and Nb$_2$GeTe$_4$: Promising thermoelectric figure of merit and gate-tunable thermoelectric performance, Nanotechnology **32**, 245203 (2021).

[15] W.-Y. Fang, P.-A. Li, J.-H. Yuan, K.-H. Xue, and J.-F. Wang, Nb$_2$SiTe$_4$ and Nb$_2$GeTe$_4$: unexplored 2D ternary layered tellurides with high stability, narrow band gap and high electron mobility, J. Electron. Mater. **49**, 959 (2020).

[16] T. Zhang, Y. Ma, X. Xu, C. Lei, B. Huang, and Y. Dai, Two-dimensional ferroelastic semiconductors in Nb$_2$SiTe$_4$ and Nb$_2$GeTe$_4$ with promising electronic properties, J. Phys. Chem. Lett. **11**, 497 (2019).

[17] W. Ju, Y. Zhang, T. Li, D. Wang, E. Zhao, G. Hu, Y. Xu, and H. Li, A type-II WSe$_2$/HfSe$_2$ van der Waals heterostructure with adjustable electronic and optical properties, Results Phys. **25**, 104250 (2021).

[18] X. Zhou, X. Sun, Z. Zhang, and W. Guo, Ferromagnetism in a semiconducting Janus NbSe hydride monolayer, J. Mater. Chem. C **6**, 9675 (2018).

[19] J. Li, Y. Li, S. Du, Z. Wang, B.-L. Gu, S.-C. Zhang, K. He, W. Duan, and Y. Xu, Intrinsic magnetic topological insulators in van der Waals layered MnBi$_2$Te$_4$-family materials, Sci. Adv. **5**, eaaw5685 (2019).

[20] Y. An, K. Wang, S. Gong, Y. Hou, C. Ma, M. Zhu, C. Zhao, T. Wang, S. Ma, and H. Wang, Nanodevices engineering and spin transport properties of MnBi$_2$Te$_4$ monolayer, npj Comput. Mater. **7**, 1 (2021).

[21] B. Radisavljevic, A. Radenovic, J. Brivio, V. Giacometti, and A. Kis, Single-layer MoS$_2$ transistors, Nat. Nanotechnol. **6**, 147 (2011).

[22] S. Kang, D. Lee, J. Kim, A. Capasso, H. S. Kang, J.-W. Park, C.-H. Lee, and G.-H. Lee, 2D semiconducting materials for electronic and optoelectronic applications: Potential and challenge, 2D Mater. **7**, 022003 (2020).

[23] Q. H. Wang, K. Kalantar-Zadeh, A. Kis, J. N. Coleman, and M. S. Strano, Electronics and optoelectronics of two-dimensional transition metal dichalcogenides, Nat. Nanotechnol. **7**, 699 (2012).

[24] G. Fiori, F. Bonaccorso, G. Iannaccone, T. Palacios, D. Neumaier, A. Seabaugh, S. K. Banerjee, and L. Colombo, Electronics based on two-dimensional materials, Nat. Nanotechnol. **9**, 768 (2014).

[25] M. Peng, Y. Tao, X. Hong, Y. Liu, Z. Wen, and X. Sun, One-step synthesized PbSe nanocrystal inks decorated 2D MoS$_2$ heterostructure for high stability photodetectors with photoresponse extend to near-infrared region, J. Mater. Chem. C **10**, 2236 (2022).

[26] W. Li, X. Qian, and J. Li, Phase transitions in 2D materials, Nat. Rev. Mater. **6**, 829 (2021).

[27] Y.-L. Hong, Z. Liu, L. Wang, T. Zhou, W. Ma, C. Xu, S. Feng, L. Chen, M.-L. Chen, D.-M. Sun, X.-Q. Chen, H.-M. Cheng, and W. Ren, Chemical vapor deposition of layered two-dimensional MoSi$_2$N$_4$ materials, Science **369**, 670 (2020).

[28] Z. Wang, X. Kuang, G. Yu, P. Zhao, H. Zhong, and S. Yuan, Electronic properties and quasiparticle model of monolayer MoSi$_2$N$_4$, Phys. Rev. B **104**, 155110 (2021).

[29] B. Mortazavi, B. Javvaji, F. Shojaei, T. Rabczuk, A. V. Shapeev, and X. Zhuang, Exceptional piezoelectricity, high thermal conductivity and stiffness and promising photocatalysis in two-dimensional MoSi$_2$N$_4$ family confirmed by first-principles, Nano Energy **82**, 105716 (2021).

[30] K. Burke, Perspective on density functional theory, J. Chem. Phys. **136**, 150901 (2012).

[31] P. Motamarri, S. Das, S. Rudraraju, K. Ghosh, D. Davydov, and V. Gavini, DFT-FE-A massively parallel adaptive finite-element code for large-scale density functional theory calculations, Comput. Phys. Commun. **246**, 106853 (2020).

[32] R. Islam, B. Ghosh, C. Autieri, S. Chowdhury, A. Bansil, A. Agarwal, and B. Singh, Tunable spin polarization and electronic structure of bottom-up synthesized MoSi$_2$N$_4$ materials, Phys. Rev. B **104**, L201112 (2021).

[33] L. Cao, G. Zhou, Q. Wang, L. Ang, and Y. S. Ang, Two-dimensional van der Waals electrical contact to monolayer $MoSi_2N_4$, Appl. Phys. Lett. **118,** 013106 (2021).

[34] L. Wang, Y. Shi, M. Liu, A. Zhang, Y.-L. Hong, R. Li, Q. Gao, M. Chen, W. Ren, and H.-M. Cheng, Intercalated architecture of MA_2Z_4 family layered van der Waals materials with emerging topological, magnetic and superconducting properties, Nat. Commun. **12,** 1 (2021).

[35] S. Smidstrup, *et al.*, QuantumATK: An integrated platform of electronic and atomic-scale modelling tools, J. Phys.: Condens. Matter **32,** 015901 (2020).

[36] X.-B. Chen and W.-H. Duan, Quantum thermal transport and spin thermoelectrics in low-dimensional nano systems: Application of nonequilibrium Green's function method, Acta Phys. Sin. **64,** 186302 (2015).

[37] J. Taylor, H. Guo, and J. Wang, Ab initio modeling of open systems: Charge transfer, electron conduction, and molecular switching of a C_{60} device, Phys. Rev. B **63,** 121104 (2001).

[38] J. M. Soler, E. Artacho, J. D. Gale, A. García, J. Junquera, P. Ordejón, and D. Sánchez-Portal, The SIESTA method for *ab initio* order-*N* materials simulation, J. Phys.: Condens. Matter **14,** 2745 (2002).

[39] S.-B. Liu, Conceptual density functional theory and some recent developments, Acta Phys. Chim. Sin. **25,** 590 (2009).

[40] Z. Y. Li, W. He, and J. L. Yang, Recent progress in density functional theory and its numerical methods, Prog. Chem. **17,** 192 (2005).

[41] M. Brandbyge, J.-L. Mozos, P. Ordejón, J. Taylor, and K. Stokbro, Density-functional method for nonequilibrium electron transport, Phys. Rev. B **65,** 165401 (2002).

[42] M. Schlipf and F. Gygi, Optimization algorithm for the generation of ONCV pseudopotentials, Comput. Phys. Commun. **196,** 36 (2015).

[43] J. P. Perdew, J. A. Chevary, S. H. Vosko, K. A. Jackson, M. R. Pederson, D. J. Singh, and C. Fiolhais, Atoms, molecules, solids, and surfaces: Applications of the generalized gradient approximation for exchange and correlation, Phys. Rev. B **46,** 6671 (1992).

[44] J. P. Perdew, K. Burke, and M. Ernzerhof, Generalized Gradient Approximation Made Simple, Phys. Rev. Lett. **77,** 3865 (1996).

[45] D. R. Hamann, Optimized norm-conserving Vanderbilt pseudopotentials, Phys. Rev. B **88,** 085117 (2013).

[46] J.-S. Yang, L. Zhao, L. Shi-Qi, H. Liu, L. Wang, M. Chen, J. Gao, and J. Zhao, Accurate electronic properties and non-linear optical response of two-dimensional MA_2Z_4, Nanoscale **13,** 5479 (2021).

[47] J. Chen and Q. Tang, The versatile electronic, magnetic and photo-electro catalytic activity of a new 2D MA_2Z_4 family, Chem. Eur. J. **27,** 9925 (2021).

[48] Y. Liu, Y. Ji, and Y. Li, Multilevel theoretical screening of novel two-dimensional MA_2Z_4 family for hydrogen evolution, J. Phys. Chem. Lett. **12,** 9149 (2021).

[49] X. Liu, H. Zhang, Z. Yang, Z. Zhang, X. Fan, and H. Liu, Structure and electronic properties of $MoSi_2P_4$ monolayer, Phys. Lett. A **420,** 127751 (2021).

[50] H. Yao, C. Zhang, Q. Wang, J. Li, Y. Yu, F. Xu, B. Wang, and Y. Wei, Novel two-dimensional layered $MoSi_2Z_4$ ($Z = P$, As): New promising optoelectronic materials, Nanomaterials **11,** 559 (2021).

[51] L.-F. Huang and Z. Zeng, Roles of mass, structure, and bond strength in the phonon properties and lattice anharmonicity of single-layer Mo and W dichalcogenides, J. Phys. Chem. C **119,** 18779 (2015).

[52] Y. An, H. Wang, J. Liao, Y. Gao, J. Chen, Y. Wu, Y. Li, G. Xu, and C. Ma, Spin transport properties and nanodevice simulations of NiI_2 monolayer, Phys. E **142,** 115262 (2022).

[53] T. Gunst, T. Markussen, K. Stokbro, and M. Brandbyge, First-principles method for electron-phonon coupling and electron mobility: Applications to two-dimensional materials, Phys. Rev. B **93,** 035414 (2016).

[54] A. V. Krukau, O. A. Vydrov, A. F. Izmaylov, and G. E. Scuseria, Influence of the exchange screening parameter on the performance of screened hybrid functionals, J. Chem. Phys. **125,** 224106 (2006).

[55] H. Wang, Z. Cheng, M. Shi, D. Ma, W. Zhuo, C. Xi, T. Wu, J. Ying, and X. Chen, Electrical transport properties of FeSe single crystal under high magnetic field, Sci. China: Phys., Mech. Astron. **64,** 1 (2021).

[56] V. Shukla, A. Grigoriev, N. K. Jena, and R. Ahuja, Strain controlled electronic and transport anisotropies in two-dimensional borophene sheets, Phys. Chem. Chem. Phys. **20,** 22952 (2018).

[57] D. Stradi, U. Martinez, A. Blom, M. Brandbyge, and K. Stokbro, General atomistic approach for modeling metal-semiconductor interfaces using density functional theory and nonequilibrium Green's function, Phys. Rev. B **93,** 155302 (2016).

[58] Y.-Y. Yang, P. Gong, W.-D. Ma, R. Hao, and X.-Y. Fang, Effects of substitution of group-V atoms for carbon or silicon atoms on optical properties of silicon carbide nanotubes, Chin. Phys. B **30,** 067803 (2021).

[59] M. Palsgaard, T. Markussen, T. Gunst, M. Brandbyge, and K. Stokbro, Efficient First-Principles Calculation of Phonon-Assisted Photocurrent in Large-Scale Solar-Cell Devices, Phys. Rev. Appl. **10,** 014026 (2018).

[60] M. Palsgaard, T. Gunst, T. Markussen, K. S. Thygesen, and M. Brandbyge, Stacked Janus device concepts: Abrupt pn-junctions and cross-plane channels, Nano Lett. **18,** 7275 (2018).

[61] B. Das and S. Mahapatra, A predictive model for high-frequency operation of two-dimensional transistors from first-principles, J. Appl. Phys. **128,** 234502 (2020).

[62] B. Das and S. Mahapatra, An atom-to-circuit modeling approach to all-2D metal–insulator–semiconductor field-effect transistors, npj 2D Mater. Appl. **2,** 1 (2018).

[63] I.-H. Lee and R. M. Martin, Applications of the generalized-gradient approximation to atoms, clusters, and solids, Phys. Rev. B **56,** 7197 (1997).

[64] T. Gunst, T. Markussen, M. L. Palsgaard, K. Stokbro, and M. Brandbyge, First-principles electron transport with phonon coupling: Large scale at low cost, Phys. Rev. B **96,** 161404 (2017).

[65] Y. An, Y. Hou, K. Wang, S. Gong, C. Ma, C. Zhao, T. Wang, Z. Jiao, H. Wang, and R. Wu, Multifunctional

lateral transition-metal disulfides heterojunctions, Adv. Funct. Mater. **30**, 2002939 (2020).

[66] H. Ai, D. Liu, J. Geng, S. Wang, K. H. Lo, and H. Pan, Theoretical evidence of the spin–valley coupling and valley polarization in two-dimensional MoSi2X4 (X = N, P, and As), Phys. Chem. Chem. Phys. **33**, 3144 (2021).

[67] Q. Li, K.-Q. Chen, and L.-M. Tang, Large Valley Splitting in van der Waals Heterostructures with Type-III Band Alignment, Phys. Rev. Appl. **13**, 014064 (2020).

[68] H. Zhong, W. Xiong, P. Lv, J. Yu, and S. Yuan, Strain-induced semiconductor to metal transition in MA_2Z_4

bilayers (M = Ti, Cr, Mo; A = Si; Z = N, P), Phys. Rev. B **103**, 085124 (2021).

[69] R. Quhe, Y. Wang, M. Ye, Q. Zhang, J. Yang, P. Lu, M. Lei, and J. Lu, Black phosphorus transistors with van der Waals-type electrical contacts, Nanoscale **9**, 14047 (2017).

[70] T. Yu, Z. Zhao, Y. Sun, A. Bergara, J. Lin, S. Zhang, H. Xu, L. Zhang, G. Yang, and Y. Liu, Two-dimensional PC_6 with direct band gap and anisotropic carrier mobility, J. Am. Chem. Soc. **141**, 1599 (2019).

[71] L. Zhang, K. Gong, J. Chen, L. Liu, Y. Zhu, D. Xiao, and H. Guo, Generation and transport of valley-polarized current in transition-metal dichalcogenides, Phys. Rev. B **90**, 195428 (2014).